**Astronomy
&
Astrophysics**

Simultaneous *XMM-Newton* and HST-COS observation of 1H0419-577

The absorbing and emitting ionized gas[*]

L. Di Gesu[1], E. Costantini[1], N. Arav[2], B. Borguet[2], R. G. Detmers[1], J. Ebrero[1], D. Edmonds[2], J. S. Kaastra[1], E. Piconcelli[3,4], and F. Verbunt[1,5]

[1] SRON Netherlands Institute for Space Research, Sorbonnelaan 2, 3584 CA Utrecht, The Netherlands
 e-mail: L.di.Gesu@sron.nl
[2] Department of Physics, Virginia Tech, Blacksburg, VA 24061, USA
[3] Osservatorio Astronomico di Roma (INAF), via Frascati 33, 00040 Monteporzio Catone, Roma, Italy
[4] XMM-Newton Science Operations Centre, ESA, PO Box 78, 28691 Villanueva de la Canada, Madrid, Spain
[5] Department of Astrophysics/IMAPP, Radboud University, PO Box 9010, 6500 GL Nijmegen, The Netherlands

Received 5 March 2013 / Accepted 14 May 2013

ABSTRACT

In this paper we analyze the X-ray, UV, and optical data of the Seyfert 1.5 galaxy 1H0419-577 with the aim of detecting and studying an ionized-gas outflow. The source was observed simultaneously in the X-rays with *XMM-Newton* and in the UV with HST-COS. Optical data were also acquired with the *XMM-Newton* Optical Monitor. We detected a thin, lowly ionized warm absorber ($\log \xi \approx 0.03$, $\log N_{\mathrm{H}} \approx 19.9$ cm^{-2}) in the X-ray spectrum, which is consistent to be produced by the same outflow already detected in the UV. Provided the gas density estimated in the UV, the outflow is consistent to be located in the host galaxy at ~kpc scale. Narrow emission lines were detected in the X-rays, in the UV and also in the optical spectrum. A single photoionized-gas model cannot account for all the narrow lines emission, indicating that the narrow line region is probably a stratified environment, differing in density and ionization. X-ray lines are unambiguously produced in a more highly ionized gas phase than the one emitting the UV lines. The analysis also suggests that the X-ray emitter may just be a deeper portion of the same gas layer producing the UV lines. Optical lines are probably produced in another disconnected gas system. The different ionization condition and the ~pc scale location, suggested by the line width for the narrow lines emitters, are evidences against a connection between the warm absorber and the narrow line region in this source.

Key words. galaxies: individual: 1H0419-577 – quasars: absorption lines – quasars: emission lines – quasars: general – X-rays: galaxies

1. Introduction

Active galactic nuclei (AGN) are believed to be powered by the accretion of matter onto a supermassive black hole (SMBH; Antonucci 1993). Emission and absorption lines in AGN spectra are the signatures of a plasma photoionized by the central source. High-resolution spectral observations can probe the physical conditions in this gas, providing information about the interaction between AGN radiation and the surrounding environment.

A variety of emission lines with different width (from 10^2 to 10^4 km s^{-1}) can be identified in AGN type 1 spectra. The diverse line broadening reflect a different location of the emitting region: narrower lines are believed to originate in a region far (~100 pc) from the black hole, which is lower in density and in temperature than the broad line region (BLR), where broader lines are emitted (Osterbrock 1989). Line emission ranges from the optical (e.g. [O III], hydrogen Balmer series) to the X-ray waveband (e.g. O VII, O VIII, Ne IX). Narrow lines may be more difficult to detect. For instance, narrow lines in the UV from e.g. C IV and O VI are blended in a dominant broad component and difficult to disentangle (e.g. Kriss et al. 2011). In the soft

X-ray, the flux of any emission line is usually outshone by the underlying continuum and lines detection is favored by a temporary low-flux state of the source (e.g. NGC 4051, Nucita et al. 2010). Whether X-ray lines arise in the same gas emitting the longer-wavelength lines is an open issue that has been recently addressed through multiwavelength photoionization modeling. In the case of Mrk 279, X-ray broad lines are consistent to be produced in a highly-ionized skin of the UV and optical BLR (Costantini et al. 2007). Bianchi et al. (2006) found that a single medium, photoionized by the central continuum, may produce the [O III] to soft X-ray ratio observed in spatially resolved images of the narrow line region (NLR).

Besides the line-emitting plasma, another photoionized gas component that can modify the spectra of type 1 AGN is a warm absorber (WA) which intervenes in the line of sight. Warm absorbers are commonly detected in about half of type 1 AGN (Crenshaw & Kraemer 1997; Piconcelli et al. 2005) via UV and/or X-ray absorption lines. These lines are usually blueshifted, (see Crenshaw et al. 2003) indicating a global outflow of the absorber. In the past ten years, multiwavelength UV-X-ray campaigns (see Costantini 2010, and references therein) have depicted the physical conditions in the outflowing gas in great detail. WA are multi component winds spanning a wide range in ionization and in velocity

---

[*] The reduced spectra as FITS files is only available at the CDS via anonymous ftp to cdsarc.u-strasbg.fr (130.79.128.5) or via http://cdsarc.u-strasbg.fr/viz-bin/qcat?J/A+A/556/A94

(e.g., Kriss et al. 2011; Ebrero et al. 2011). X-ray spectra show the the most highly ionized lines (e.g., from O VII, O VIII and Ne IX), while a lower ionization phase (e.g., C II, Mg II) is visible only in the UV. In some cases (e.g., NGC 3783, NGC 5548, NGC 4151, Mrk 279), a common phase producing e.g. O VI lines in both the UV and the X-ray spectrum has been identified (Kaspi et al. 2002; Steenbrugge et al. 2005; Kraemer et al. 2005; Arav et al. 2007). Similarities in the line width (NGC 3783, Behar et al. 2003) and in the gas column density (NGC 5548, Detmers et al. 2009) suggest a connection between the WA and the gas in the NLR. However, the origin of WA is not clearly established yet, mainly because of the great uncertainty in estimating its location.

Provided the gas density, the distance of the outflow from the central source can be in principle derived from the gas ionization parameter $\xi = L_{ion}/nR^2$ (where L_{ion} is the source ionizing luminosity, n is the gas density, and R is the distance from the ionizing source). However, the gas density in most cases is unknown, and the distance may just be estimated indirectly (Blustin et al. 2005). Absorption lines from collisionally excited metastable levels may provide a direct density diagnostic (e.g. Bautista et al. 2009), but they are rarely detected. In the UV, metastable lines from e.g. Fe II, Si II, and C II have been detected in a handful of cases (e.g. Moe et al. 2009; Dunn et al. 2010; Borguet et al. 2012). In the X-rays the identification of metastable lines from O V is hampered by uncertainties in the predicted line wavelength (Kaastra et al. 2004). So far, available estimations, using different methods, have located the outflows within the BLR (e.g., NGC 7469, Scott et al. 2005) or have located them as far as the putative torus (e.g. Ebrero et al. 2010). In some quasars, a galactic scale distance has been reported (Hamann et al. 2001; Hutsemékers et al. 2004; Borguet et al. 2012; Moe et al. 2009).

The distance estimation allows quantifies the amount of mass and energy released by the outflow into the medium. Hence, it is possible to establish, if WA contributes to the AGN feedback, which is often invoked to explain the energetics and the chemistry of the medium to a very large scale (Sijacki et al. 2007; Hopkins et al. 2008; Somerville et al. 2008; McNamara & Nulsen 2012). Warm absorbers usually produce a negligible feedback (e.g. Ebrero et al. 2011). Only the fastest AGN wind (e.g. Moe et al. 2009; Dunn et al. 2010; Tombesi et al. 2013) may be dynamically important in the evolution of the interstellar medium (Faucher-Giguère & Quataert 2012).

In this paper, we analyze a long-exposure *XMM-Newton* dataset of the bright Seyfert galaxy 1H0419-577, which was taken simultaneously with a Cosmic Origins Spectrograph (HST-COS) spectrum. The source is a radio-quiet quasar located at redshift $z = 0.104$ and is spectrally classified as a type 1.5 Seyfert galaxy (Véron-Cetty & Véron 2006). Using the Hβ line width, Pounds et al. (2004b) derived a $1.3 \times 10^8\ M_\odot$ mass for the SMBH hosted in the nucleus. The HST-COS spectrum has been published by Edmonds et al. (2011, herafter E11). The UV spectrum displays broad emission lines from C IV, O VI, and Ly α and absorption lines (E11). Three outflowing components were identified in absorption with the line centroids located at $v_1 = -38\ km\ s^{-1}$, $v_2 = -156\ km\ s^{-1}$, and $v_3 = -220\ km\ s^{-1}$ in the rest frame of the source. Only a few ionized species (H I, C IV, N V, O VI) were detected in component 1, while component 2 + 3 displays a handful of transitions from both low (e.g., C II) and high-ionization species (e.g. C IV, N V, O VI).

The present analysis is focused mainly on the high-resolution spectrum collected with the Reflection Grating Spectrometer (RGS, den Herder et al. 2001); in a companion paper, we will

Table 1. *XMM-Newton* observation log for 1H0419-577.

Observation ID	0604720401	0604720301
Date	28/05/2010	30/05/2010
Orbit	1917	1918
Net exposure (ks)[a]	61	97
RGS Count Rate (s^{-1})	0.337 ± 0.002	0.385 ± 0.002
EPIC-pn Count Rate (s^{-1})	1.41 ± 0.02	1.56 ± 0.02

Notes. [a] Resulting exposure time after correction for flaring.

present the broad band X-ray spectrum of this source. Analysis of a previous RGS dataset is reported in Pounds et al. (2004a). Hints of narrow absorption features from an Fe unresolved transition array (UTA) were noticed in the spectrum. However, the short exposure time (~15 ks) has so far prevented an unambiguous detection and characterization of a WA in this source.

The paper is organized as follows: in Sect. 2, we present the *XMM-Newton* observations and the data reduction; in Sect. 3, we describe the spectral energy distribution of the source; in Sect. 4, we discuss the spectral analysis; in Sect. 5, we model the narrow emission lines of the source; in Sect. 6, we compare the X-ray and the UV absorber; in Sect. 7, we discuss our results and in Sect. 8, we finally present the conclusions. The cosmological parameters used are: $H_0 = 70\ km\ s^{-1}\ Mpc^{-1}$, $\Omega_m = 0.3$ and $\Omega_\Lambda = 0.7$. Errors are quoted at 68% confidence levels ($\Delta\chi^2 = 1.0$) unless otherwise stated.

2. Observations and data preparation

In May 2010, two consecutive exposures of 1H0419-577 were taken with the *XMM-Newton* X-ray telescope with both the EPIC cameras (Strüder et al. 2001; Turner et al. 2001) and the RGS. Moreover, optical monitor (OM, Mason et al. 2001) imaging mode data were acquired with four broad-band filters (*B*, *UVW1*, *UVM2*, *UWV2*) and two grism filters (Grism1-UV and Grism2-visual). The source was observed for ~167 ks in total, and a slight shift in the dispersion direction was applied in the second observation. In this way, the bad pixels of the RGS detectors were not at the same location in the two observations, allowing us to correct them by a combination of the two spectra (see Sect. 2.1). Details of the two observations are provided in Table 1.

2.1. The RGS data

For both RGS datasets, we processed the data following the standard procedure[1] using the *XMM-Newton* Science Analysis System (SAS, version 10.0.0) and the latest calibration files. We created calibrated event files for both RGS1 and RGS2, and to check the variation of the background, we also created the background light curves from CCD 9. The background of the first observation was quiescent, while the second light curve showed contamination by soft protons flares. We cleaned the contaminated observation by applying a time filter to the event-files: for this purpose, we created the good time intervals (GTI) by cutting all the time bins in the light curve where the count rate was over the standard threshold of 0.2 counts s^{-1}. Resulting exposure time after deflaring is 97 ks. Starting from the cleaned event files, we created a fluxed spectrum for each RGS detector for both observations. We did this through the SAS task rgsfluxer,

---

[1] http://xmm.esac.esa.int/sas/8.0.0/documentation/threads/

considering only the first spectral order and correcting for the background.

The spectral fitting for 1H0419-577 was performed using the package SPEX, version 2.03.02 (Kaastra et al. 1996). We first fit the RGS spectrum of each observation to check whether the continuum was unchanged in the two datasets: we found that the continuum could be phenomenologically fitted by a broken power law in both datasets. The variations of the fitted parameters were within the statistical errors. Moreover, the measured flux in the RGS bandpass was basically the same (within ∼8%) in the two observations. This source is well known in the literature for being highly variable in the soft X-ray band (<2.0 keV) (e.g. Pounds et al. 2004b): our observation caught it in an intermediate flux state ($F_{0.5-2.0 \, \mathrm{keV}}^{\mathrm{pn}} \approx 10^{-11}$ erg s^{-1} cm^2).

Given the stability of the continuum shape in the two observations, we could safely perform a combination of the spectra to improve the signal to noise ratio. We followed the same route outlined in Kaastra et al. (2011); here we just summarize the main steps. We combined the four fluxed spectra created with rgsfluxer into a single stacked spectrum using the SPEX auxiliary program *RGS_fluxcombine*. The routine *RGS_fluxcombine* sums up two spectra using the exposure time to weigh all the bins without bad pixels. In the presence of a bad pixel, this procedure is incorrect since it would create an artificial absorption line (for an analytical example see, Kaastra et al. 2011). To correct the output spectrum from bad pixels, the task works as follows: in the presence of a bad pixel, it looks at the neighbouring pixels and, assuming that the spectral shape does not change locally, it estimates the contribution to the total flux expected from good data. Using this fraction, the task estimates the factor by which the flux at the bad pixel location has to be scaled. For the final composite spectrum, the proper SPEX readable response matrix was hence created through the tool *RGS_fmat*.

2.2. The OM data

We retrieved the processing pipeline subsystem (PPS) products of the OM Image Mode operations to extract the source count rates in four broadband filters: *B* (λ_{eff} = 4340 Å), *UVW1* (λ_{eff} = 2910 Å), *UWM2* (λ_{eff} = 2310 Å), and UVW2 (λ_{eff} = 2120 Å). Hence, we converted the count rates to flux densities using the conversion factors provided in the SAS watchout web page[2].

We also processed the images from the OM optical grism using the standard reduction pipeline (omgchain) provided in the SAS. The task corrects the raw OM grism files from the Modulo-8 fixed pattern noise and removes the residual scattered light features. It rotates the images, aligning the grism dispersion axis to the pixel readout columns of the images, and it runs a source detection algorithm. Finally, the tool extracts the spectra of the detected sources from the usable spectral orders. A step-by-step description of the grism extraction chain is given in the SAS User's Guide. For the present analysis, we used the 5 ks long optical spectrum (grism1, first dispersion order) from the dataset 0604720301 to measure the luminosities of the optical narrow emission lines of 1H0419-577 (Sect. 4.4).

2.3. The EPIC data

To constrain the spectral energy distribution (SED) of the source in the X-ray band, we used the broadband EPIC-pn spectrum.
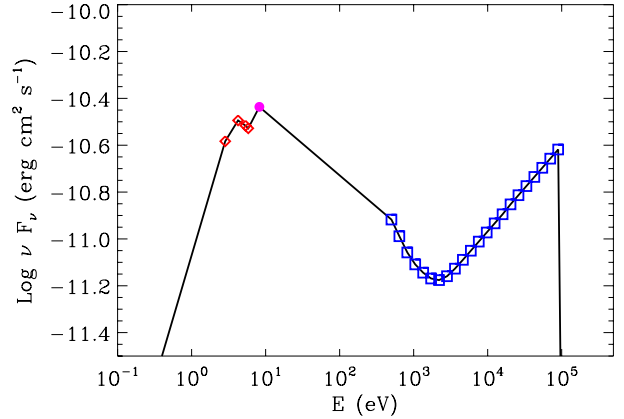
Fig. 1. Spectral energy distribution for 1H0419-577. Open diamonds are the fluxes from the OM optical and UV broad band filters discussed in the text. The filled circle is the continuum flux taken from the simultaneous HST-COS observation. Open squares are from the unabsorbed model for the X-ray continuum, observed with the EPIC-pn.

We applied the standard SAS data analysis thread to the observation data files (ODF) products of both observations. We created the calibrated EPIC-pn event files, and we cleaned them from soft proton flares through a time filtering of the light curves. The counts threshold over which we discarded the time bins of the light curves was determined by a 2σ clipping of the light curve in the whole EPIC band. Starting from the clean event files we extracted the source and background spectra and we created the spectral response matrices. We fitted the EPIC-pn spectrum with a phenomenological model, considering the effect of the galactic absorption. The unabsorbed phenomenological continuum model of the EPIC-pn spectrum served as input for the X-ray SED.

3. The spectral energy distribution

We exploited the simultaneous *XMM-Newton* and HST-COS observation to constrain the SED of source. The shape of the SED at lower energy is constrained by the *XMM-Newton* OM and by HST, while the EPIC-pn camera covers the higher energy range. For this purpose, we estimated the UV continuum of the source at 1500 Å in the complete HST-COS spectrum. We selected a wavelength region that was not contaminated by any emission lines (1495–1505 Å), and we averaged the 83 spectral points comprised in it.

We cut off the SED at low ($E \leq 1.36$ eV) and high energy ($E \geq 100$ keV). Indeed, the AGN SED falls off with the square of the energy above 100 keV, while the optical-UV bump has an exponential cutoff in the infrared (Ferland et al. 2003). We show the SED in Fig. 1. From a numerical integration of the SED, we calculated the source bolometric luminosity (log L_{bol} = 45.95 erg s^{-1}): for the SMBH hosted in 1H0419-577, the Eddington ratio is therefore $L_{\mathrm{bol}}/L_{\mathrm{Edd}}$ = 0.5. The source ionizing luminosity in the $1-1000$ Ry energy range is log L_{ion} = 45.43 erg s^{-1}.

4. Spectral analysis

4.1. RGS continuum fitting

We show the composite RGS spectrum of 1H0419-577 in Fig. 2. We fitted the spectrum in the $8-38$ Å band, and we applied a factor 5 binning. Because the (more appropriate) C-statistic cannot
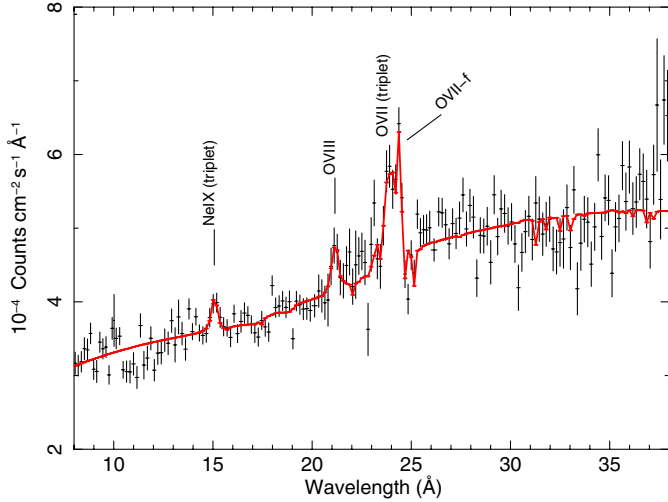
Fig. 2. Composite RGS spectrum of 1H0419-577. We rebinned the spectrum for clarity. The solid line corresponds to the best-fit model. The main emission features are labeled.

be computed in the case of our combined fluxed spectrum, we used the χ^2 statisticfor the fit. We checked that at least 20 counts were collected in each spectral bin, as required for using the χ^2 statistic. We consider the cosmological redshift and the effects of Galactic neutral absorption. For the latter, we used the HOT model (collisional ionized plasma) in SPEX, considering a column density of $N_H = 1.26 \times 10^{20}$ cm^{-2} (Kalberla et al. 2005) along the line of sight and a temperature of 0.5 eV to mimic a neutral gas.

We modeled the continuum emission with a broken power law. The best-fit parameters that we obtained are $\Gamma_1 = 2.73 \pm 0.02$ and $\Gamma_2 = 2.30 \pm 0.03$ as indexes with a break energy of $E_0 = 0.80 \pm 0.03$ keV.

4.2. RGS emission lines

Superposed on the underlying continuum, the spectrum exhibits emission lines, of which most are broadened. To model the broad emission features of the spectrum, we added a Gaussian to the fit for each candidate emission line, leaving the centroid, the linewidth and the flux as free parameters. We also tested the significance of the improvement of the χ^2_ν given by the extra component through an F-test. The F-test is trustworthy in testing the presence of an emission line if the line normalization is allowed to vary also in the negative range (Protassov et al. 2002).

We show the results in Table 2. Three broad components gave a highly significant improvement of the fit. Beside the Ne IX blended triplet and the O VIII Ly α line, that are redshifted respectively at ~15.1 Å and ~21.2 Å (Fig. 2), the most prominent broad emission feature we detected in the spectrum is a blend of the lines of the O VII triplets. In Fig. 3, we provide a zoom on the 20−26 Å spectral region, where O VII and O VIII lines are seen. To fit the spectrum in this complex region, we first modeled the prominent narrow line visible at ~24.4 Å with a delta function, finding a rest wavelength of 22.11 ± 0.08 Å for it. Therefore, we could identify this line as due to the forbidden transition of O VII: the line is formally detected with the F-test giving a significance above 99.99%. The line was unresolved, but we could however estimate un upper limit for its line width. Assuming a 3:1 value for the forbidden-to-intercombination line ratio (Porquet & Dubau 2000), we

Table 2. Parameters of 1H0419-577 X-ray broad lines.

Ion[a]	Rest wavelength[b] Å	$\log(L_{obs})$[c] erg s^{-1}	*FWHM*[d] km s^{-1}	F-test[e]
O VII	21.69 ± 0.07	42.44 ± 0.07	$11\,000 \pm 1000$	>99.99%
O VIII	19.17 ± 0.06	41.95 ± 0.16	5000 ± 2000	99.2%
Ne IX	13.66 ± 0.05	41.81 ± 0.15	5000 ± 3000	99.6%

Notes. [a] Line transition. Note that O VII and Ne IX are blends. [b] Wavelength of line centroid in the local frame. [c] Intrinsic line luminosity. [d] Line Doppler broadening as given by the full width at half maximum of the fitted Gaussian. [e] Line significance as given by the F-test probability.

provided the intercombination and resonance lines that corresponds to the detected O VII-f line. After adding these two narrow lines, the spectrum was still poorly fitted in the 23.5−24.5 Å range, showing broad prominent residuals. Hence, we added a broad-line to the fit leaving the centroid free to vary in the range among the known transitions of the O VII triplets. The modeling of the oxygen emission features allows a proper detection of any intervening absorption system (e.g. Costantini et al. 2007). Indeed, transitions from O IV-O VII are in principle present in the same wavelength region covered by the blend of the O VII lines.

Beside the O VII-f line, we determined upper limits for the luminosity of several other narrow lines. Since the narrow line width is not resolved in the RGS spectrum, we modeled them with a delta function. We estimated the upper limits by determining the maximum normalization below which a delta line centered at the wavelength of the known transition is undetectable over the continuum. The parameters of the X-ray narrow lines are listed in the upper panel of Table 4.

4.3. RGS absorption lines

We modeled the X-ray absorbing gas of 1H0419-577 using the photoionized-absorption model XABS in SPEX. This model calculates the transmission of a slab of material, where all ionic column densities are linked through the ionization balance. Thus, it computes the whole set of absorption lines produced by a photoionized absorbing gas for a gas column density N_H and an ionization parameter ξ. The gas outflow velocity v_{out} is another free parameter. We set instead the RMS velocity broadening of the gas to the default value (100 km s^{-1}). The input ionization balance for XABS is sensitive to the spectral shape of ionizing SED: we calculated it running the tool *xabsinput* with the SED described in Sect. 3 as input. The *xabsinput* routine makes use internally of the Cloudy code (ver. 10.00, Ferland et al. 1998) to determine the ionization balance. In the calculation, we assume solar abundances as given in Cloudy (see Cloudy manual[3] for details). We found that the absorption features of 1H0419-577 can be fitted by a thin and lowly-ionized absorber. The best-fit parameters are $N_H = 8 \pm 3 \times 10^{19}$ cm^{-2} and $\log \xi = 0.03 \pm 0.15$. We had no strong constraints on a possible outflow velocity. We estimated an upper limit at 99% confidence ($\Delta\chi^2 = 6.67$ for one parameter) of $v_{out} \leq 210$ km s^{-1}. By adding the absorption component, we achieved an improvement of the statistic of $\Delta\chi^2 = 25$ for 3 extra degrees of freedom. According to the F-test, this χ^2 improvement is significant at a 99.7% level of confidence. The most prominent absorption lines (Fig. 3) are transitions from lowly ionized oxygen species, such as O IV and O V, redshifted
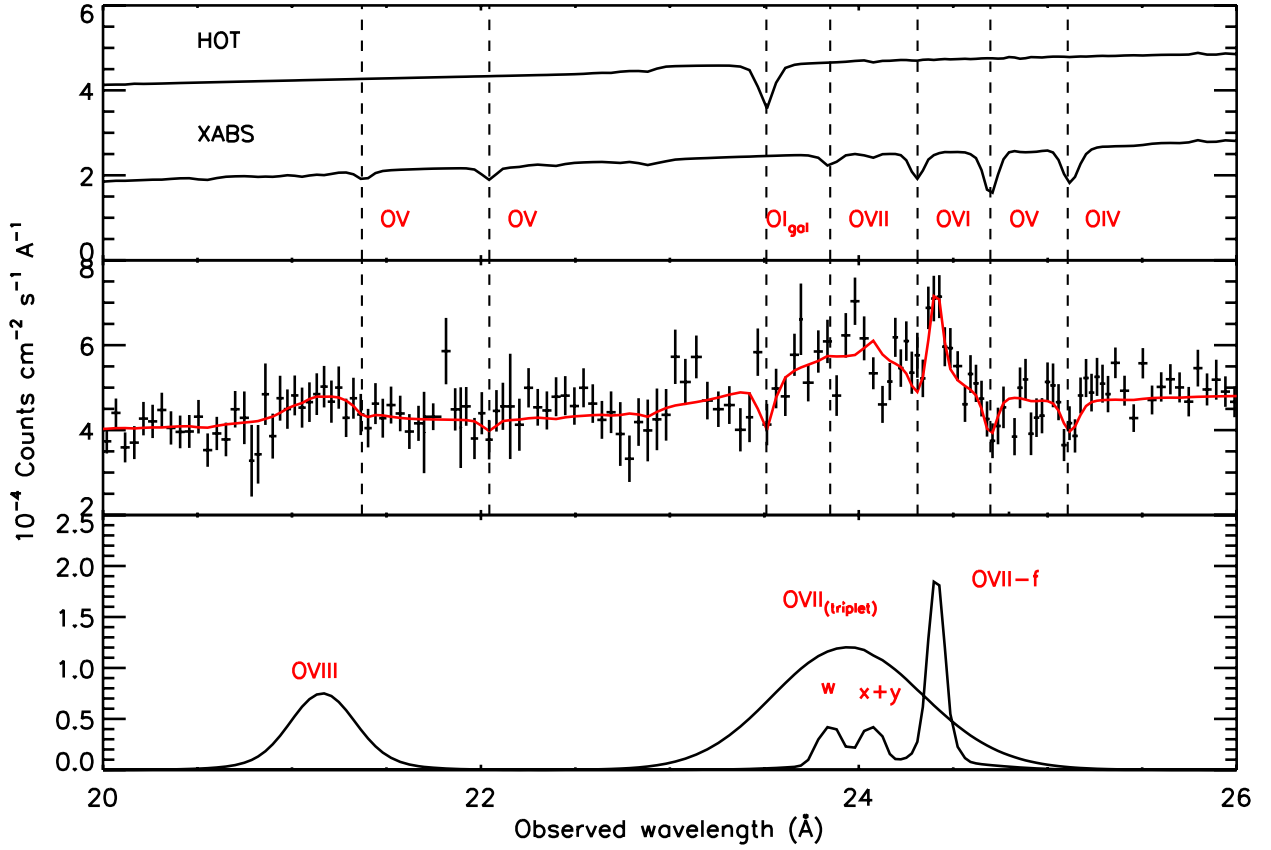
---

[3] http://nublado.org/

Fig. 3. *Middle panel*: best fit to the RGS spectrum of 1H0419-577 in the 20−26 Å wavelength range. *Upper panel*: absorbing components. The neutral absorbers at $z = 0$ and the local WA (shifted downward for plotting purpose) are displayed as solid lines. *Lower panel*: profiles of the broad and narrow emission features.

Table 3. Column densities of the main absorbing ions for 1H0419-577.

Ion	XABS[a] $\log (N_{ion})$ cm^{-2}	SLAB[b] $\log (N_{ion})$ cm^{-2}
O IV	16.2 ± 0.1	16.1 ± 0.2
O V	16.2 ± 0.1	16.4 ± 0.4
O VI	15.9 ± 0.1	≤ 15.6
O VII	15.2 ± 0.1	15.9 ± 0.5
C V	16.1 ± 0.1	≤ 16.8
N IV	15.3 ± 0.1	≤ 15
N V	15.3 ± 0.1	$15.4^{+0.4}_{-1.7}$
N VI	15.3 ± 0.1	≤ 15.5

Notes. [a] Ionic column densities provided by the XABS model. Quoted errors are from the propagation of the error on the fitted hydrogen column density. [b] Ionic column densities from the line-by-line fitting performed with the SLAB model.

to 25.1 Å and 24.7 Å (Fig. 3). respectively. In Table 3, we provide the column densities, predicted by XABS, of the main ions of the absorber. As a comparison, we also fitted each ionic column density individually with the SLAB model. SLAB is a simpler absorption model where all the ionic column densities are modeled independently, since they are not linked each other by any photoionization model. In the line-by-line fit with SLAB, we kept the same outflow velocity and velocity broadening of the previous XABS fit. XABS predictions and SLAB fit are consistent within the quoted errors. Therefore, we will use hereafter the value provided by XABS as reference.

Table 4. Parameters of the X-ray, UV, and optical narrow lines of 1H0419-577.

Ion	Wavelength[a] Å	$\log (L_{obs})$[b] erg s^{-1}	FWHM[c] km s^{-1}
C VI	33.73	≤ 41.67	...
N VI	29.53	≤ 40.73	...
N VII	24.78	≤ 40.65	...
O VII-f	22.11 ± 0.08	41.84 ± 0.08	≤ 2500
O VIII	18.97	≤ 41.69	...
Ne IX	13.70	≤ 40.52	...
C IV	1551	42.89	805 ± 40
C IV	1548	43.03	805 ± 40
Ly α	1215	43.18	488 ± 24
O VI	1038	42.69	840 ± 42
O VI	1032	42.73	840 ± 42
[O III]	5007	43.13 ± 0.01	1200 ± 100
[O III]	4959	42.71 ± 0.03	500 ± 300
Hβ	4861	42.14 ± 0.12	488 (fixed)

Notes. Parameters and errors for the X-ray, UV, and optical narrow emission lines of 1H0419-577. [a] Wavelength of the transition in the rest frame. [b] Intrinsic line luminosity. [c] Doppler broadening of the line, as given by the full width at half maximum of the fitted Gaussian. Note that the X-ray lines are not resolved in the RGS spectrum.

4.4. The UV and optical narrow emission lines

We also studied the narrow emission-lines present in both the optical and the UV spectrum. In the middle panel of Table 4, we list the UV narrow emission lines derived from the fit performed
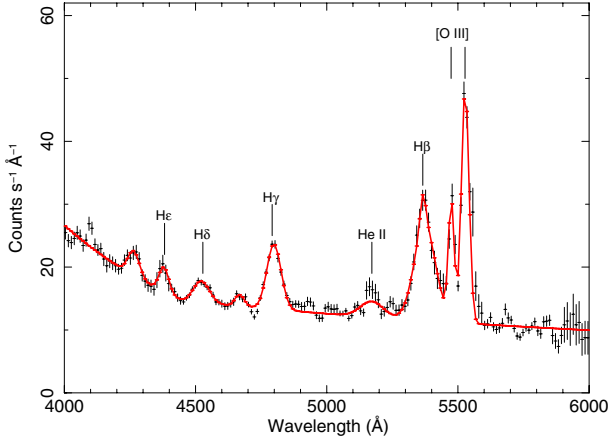
Fig. 4. OM optical grism spectrum of 1H0419-577 in the 4000–6000 Å range. The best-fit model is displayed by a solid line. The main emission features from the hydrogen Balmer series an the [O III] doublet are labeled.

Table 5. Covering factor, column density and ionization parameter for the gas emitting the UV and X-ray narrow lines in 1H0419-577.

	C_v	$\log N_{\rm H}$ cm^{-2}	$\log \xi$
UV[a]	0.104 ± 0.006	21.67 ± 0.25	0.48 ± 0.15
X[b]	0.104 (fixed)	21.40 ± 0.25	1.44 ± 0.15

Notes. [a] Best-fit parameters for the gas emitting the UV lines; [b] Parameter of the gas model consistent with the observed upper limits and best-fit of the only detected X-ray line. We imposed the same gas covering factor of the UV-emitter. See text for details.

on the simultaneous HST-COS spectrum. Each line was fitted by a combination of resolved broad and narrow components (see Sect. 3.1 and Fig. 2 in E11 for details). From the parameters of the fit, a formal 5% error was estimated on the narrow component, for both the line luminosity and line width. This error does not include any uncertainty associated to the blend of the narrow and the broad components.

Finally, the lower panel of Table 4 lists the optical narrow emission lines, which were obtained by fitting the OM grism spectrum (Fig. 4). We fitted the continuum with a broken power-law, and we modeled the sinusoidal feature that was due to a residual Modulo-8 fixed pattern noise with Gaussians. We clearly detected the broadened features of the hydrogen Balmer series (Hβ λ4861 Å, Hγ λ4341 Å, Hδ λ4102 Å and Hϵ λ3970 Å) and the narrow emission lines of the [O III] doublets $\lambda\lambda$5007, 4959 Å. In the analysis, we used the luminosities of the [O III] lines and of the narrow component of Hβ. We modeled the [O III] lines with Gaussian profiles, leaving the centroid, the line width, and the flux as free parameters. The full width at half maximum (*FWHM*) of the [O III] lines was resolved, and it is reported in Table 4. In fitting the Hβ line, we used two Gaussians, respectively, for a narrow and a broad component. We set the wavelength of the narrow component to the nominal wavelength of the Hβ transition and its width to that of the Ly α narrow component measured in the UV, leaving only the normalization as free parameters. All the parameters of the broad component were otherwise left free. The fitted *FWHM* for the broad Hβ component (4700 ± 400 km s^{-1}) is within the range of the three broad components of Ly α measured in the UV spectrum ($\approx$1000, 3400, and 14 000 km s^{-1}).

5. Photoionization modeling

To estimate the global properties of the gas that emits the narrow lines in 1H0419-577, we used the photoionization code, Cloudy v. 10.0 (Ferland et al. 1998). In the calculation, we assumed total coverage of the source and a gas density of 10^8 cm^{-3}. We note that the assumption on the gas density is not critical for the resulting gas parameters. Indeed, line ratios of He-like ions are not sensitive to the gas density over a wide range of density values (Porquet & Dubau 2000). We used the SED described in Sect. 3 and the ionizing luminosity derived from it as input. We created a grid of line luminosities for a wide range

of possible gas parameters: the column density ranged between $\log N_{\rm H} = [19-23]$ cm^{-2} and the ionization parameter between $\log \xi = [-0.3-2.7]$ erg cm s^{-1} with a spacing of 0.25 dex and 0.15 dex, respectively. In the fitting routine, we first computed the gas covering factor C_v for each grid entry by imposing to the model to match the luminosity of the Ly α line. Hence, we modeled the data by minimizing the merit function:

$$\chi^2 = \sum \frac{(C_v L_c - L_{\rm obs})^2}{\sigma_{\rm obs}^2},$$

where L_c is the model-predicted luminosity of each line, C_v is the gas covering factor, and $L_{\rm obs}$ is the observed line luminosity with statistical error $\sigma_{\rm obs}$. We fitted all the UV, X-ray, and optical luminosities listed in Table 4. The C IV, O VI, and [O III] doublets were considered as a blend, and 3σ upper limits for the X-ray lines of Table 4 were also included.

A model with a $\sim$10% covering factor, $\log N_{\rm H} \sim 21.67$ cm^{-2} and $\log \xi \sim 0.48$ fits the three UV data points (Ly α, C IV, O VI) and agrees with all the upper limits for the X-ray luminosities. In fitting the UV lines we obtain a minimum χ^2/d.o.f. = 0.35/1. With just one degree of freedom the probability of getting a low or lower observed χ^2 for a correct model is 0.45. The derived parameter for the UV emitter are outlined in Table 5. We report the width of the grid step as error on the parameters. The error for the covering factor is estimated by propagating the error ($\sim$5%) on the luminosity of the Ly α line.

This best-fit model neither matches the luminosity of the O VII-f nor the luminosities of the optical lines, suggesting that X-ray and optical lines arise in a gas with different physical conditions. It was not possible to estimate the parameters of the X-ray emitter through a proper fit, because we had only one line detection. However, the measured upper limits provide useful constraints for the model. Assuming the same covering factor of the UV emitter, we selected all the models in the grid that agree with the measured upper limits and match the luminosity of the O VII-f line within 3$\sigma_{\rm obs}$. In this calculation, we added the contribution of the best-fit UV model to the X-ray luminosities. We find that the selected models have $\log N_{\rm H}$ ([21.13–21.93] cm^{-2}) and their ionization parameter is comprised within $\log \xi = [1.12-2.06]$. Therefore, the fit that best models the O VII-f line has a column density consistent within a grid step with the UV emitter one ($\log N_{\rm H} \approx 21.40$ cm^{-2}) but its ionization parameter is ($\log \xi \approx 1.44$). This may indicate a geometrical connection between the UV and the X-ray emitter. In the case when also the gas covering factor is left free, we obtained a broader parameter range, ($C_v = [0.03-0.60]$, $\log N_{\rm H} = [20.90-23.00]$ cm^{-2}), which still indicates a higher ionization parameter ($\log \xi = [1.12-1.60]$) with respect to the UV-emitter. We also remark that none of the models in our grid match the optical-lines luminosities. Finally, we note that
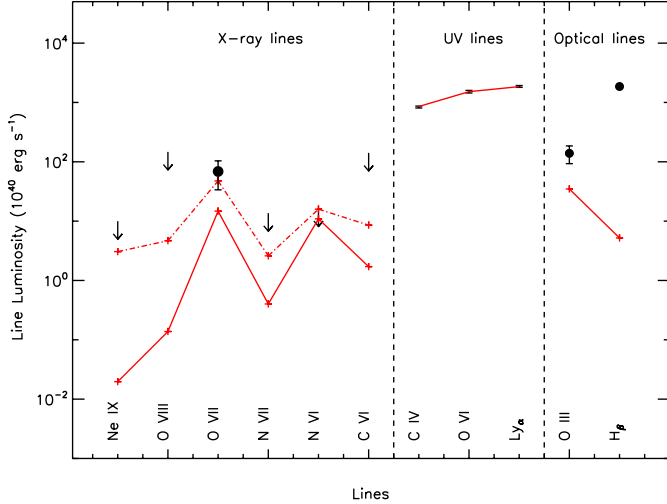
Fig. 5. Best fit of the intrinsic luminosities of the UV narrow emission lines (*middle panel*). The model is displayed by a solid line only to guide the eye. The line luminosities predicted by the model in the X-ray (*left panel*) and in the optical (*right panel*) band are displayed by red crosses connected by a solid line. The model agrees with the upper limits for the X-ray lines but does not fit the optical lines. The qualitative best fit model for the X-ray lines is also shown by red crosses connected by a dot dashed line. Error bars, when larger than the size of the plotting symbols, are also shown. Note that a 3σ error bar is shown for O VII-f line.

models with parameters consistent with the WA detected in the RGS spectrum neither fit the UV ($\chi^2 = [246-631]$) nor the X-ray (the O VII-f is not fitted within $\approx 6\sigma$) emission lines. We show the best-fit models for the UV and the X-ray emission lines in Fig. 5. The derived parameter for the X-ray emitter are outlined in the second row of Table 5.

6. Comparison between the UV and the X-ray absorber

We investigate the possible relationship between the UV absorber found for 1H0419-577 in E11 and the X-ray absorber found here (Sect. 4.3) by comparing the gas parameters independently measured in the two different wavebands.

Three different outflow components ($v_1 = -38\,\mathrm{km\,s^{-1}}$, $v_2 = -156\,\mathrm{km\,s^{-1}}$, and $v_3 = -220\,\mathrm{km\,s^{-1}}$) were identified in the UV. Because of the the lower RGS resolution, we were not able to resolve any of the UV components; however our upper limit for the outflow velocity of the X-ray absorber is consistent with all of them. Thus, it is likely that we observed a blended superposition of the UV components in the X-rays.

In Table 6, we compared the UV and X-ray column densities for C II, C IV, N V, and O VI. Absorption lines from O VI were detected in both bands, while lines from C II, C IV, and N V were detected only in the UV; their column densities however could be predicted by our XABS model. We report the sum of the column densities of the UV kinetic components 1, 2, and 3, in Table 6. These were obtained using a UV partial covering model, with a power law distribution of the optical depth (see E11 for details). The column densities independently found in the X-ray and the UV agree within the quoted error range for all ions.

The ionization parameter of the UV absorber is given in terms of $U_H = \frac{Q_H}{4\pi R^2 c N_H}$ (where Q_H is the rate of ionizing photons emitted by the source, R is the absorber distance from the source, c is the speed of light, and N_H is the total hydrogen column

Table 6. Comparison between the UV and X-ray column densities of the absorbing ions in 1H0419-577.

Ion	UV[a] $\log(N_{ion})$ cm^{-2}	X[b] $\log(N_{ion})$ cm^{-2}
C II	12.99−13.08	13.11
C IV	15.16−15.29	15.42
N V	15.16−15.31	15.36
O VI	15.83−15.96	15.89

Notes. [a] Ionic column densities measured in the UV. We considered the sum of the three kinetic components detected. [b] Ionic column densities predicted the X-ray model (XABS), as discussed in Sect. 4.3.

density), while we used ξ as defined in Sect. 1. For the SED of 1H0419-577, $\log\xi = 1.7 + \log U_H$. In the UV, the determination of U_H is not well constrained: for a broken power law SED and for a gas with solar abundances, $\log U_H = [-1.7$ to $-1.5]$ (Fig. 8 in E11). Applying the conversion factor just given, this value corresponds to $\log\xi = [0$ to $0.2]$, which is consistent with the more constrained value found here for the X-ray absorber: $\log\xi = [-0.12$ to $0.18]$.

7. Discussion

7.1. Absorber distance and energetics

The spectral analysis of the RGS spectrum of 1H0419-577, together with the analysis of the simultaneous COS spectrum (E11), revealed that the X-ray and the UV emission spectra of 1H0419-577 are both absorbed by a thin, weakly ionized absorber. As pointed out in Sect. 6 the ionization parameter and the ionic column densities independently measured in the UV and the X-ray agree with each other. Thus, it is likely that the UV and X-ray WA are the same gas. In the UV, the kinetic structure of the WA is resolved, with three outflowing components detected. The bulk of absorbing column density is carried by components 2+3 (see Tables 1 and 2 and Fig. 3 in E11). Therefore, we likely detected a blend of the UV kinetic components dominated by the UV components 2+3 in the lower resolution X-ray spectrum. Having established the connection between the UV and the X-ray absorber, we can exploit the complementary information derived in the two wavebands to estimate the WA location and energetics.

In the following discussion, we consider that an ionized medium, parameterized by $\log\xi \approx 0.03$ and $N_H \approx 8 \times 10^{19}\,\mathrm{cm}^{-2}$ (this paper), is outflowing from the source at the velocity of UV component 3 ($v_3 = -220\,\mathrm{km\,s^{-1}}$). Additionally, we use a gas number density $n_H \leq 25\,\mathrm{cm}^{-3}$, as estimated in E11 for the UV component 2+3. This upper limit for the gas number density was derived from the ratio of the (nondetected) first excited metastable and the ground level of C II. As already pointed out in Sect. 6, the C II column density measured in the UV is well accounted for by our absorber model. We note however that the C II 1334.5 Å profile is possibly asymmetric in the COS spectrum, and the centroid is slightly shifted with respect to the UV component 3: at least part of the C II emission may in principle arise in a kinetic component that is separated from the UV component 3. However, this possible additional component is not evident in any other lines.

Given the X-ray/UV connection just established, the following discussion is based on the assumption that the upper limit for the gas density estimated in the UV may be applied to the

UV/X-ray absorber. We assume a thin shell geometry for the outflow. In this approximation, the outflow is spherically shaped with a global covering factor of the line of sight C_g. Each outflowing shell, Δr thick, is partially filled with gas, with a volume filling factor f. The volume filling factor f can be estimated analytically (Blustin et al. 2005) from the condition that the kinetic momentum of the outflow must be on the order of the momentum of the absorbed radiation plus the momentum of the scattered radiation. Applying this condition, we found that the absorber in 1H0419-577 has a volume filling factor $f \approx 3 \times 10^{-3}$, suggesting that it may consist of filaments or fragments that are very diluted in the available volume and intercepting our line of sight.

Exploiting the tighter constraint on the ionization parameter provided by the present analysis we confirm the distance estimation given in E11:

$$R \geq \left(\frac{L_{ion}}{n_H \xi}\right)^{1/2} \gtrsim 3 \, \text{kpc}. \tag{1}$$

This estimation places the WA at the host galaxy scale, well outside the central BLR ($R_{BLR} \approx 0.07$ pc, Turner et al. 2009). UV absorbers located at a galactic-scale distance are not uncommon in low-redshift quasars (see Table 6 in E11 and references therein). The X-ray/UV connection that we infer for this source would therefore make its low-ξ absorber the first galactic scale X-ray absorber ever detected. A possible confining medium for an X-ray absorbers located at about a ~kpc from the nucleus could be a radio jet-like emission. This source is radio quiet, but a 843 MHz flux detection (Mauch et al. 2003) may be due to a weak radio lobe. More accurate radio measurements are required to test this possibility. This a galactic-scale wind may be both AGN or starburst driven. However, the UV analysis for this source, suggests that the photoionization of the outflow may be dominated by the AGN emission (see discussion in E11 and references therein).

We also estimated an upper limit for the WA distance from the condition that the thickness Δr of the outflowing-gas column should not overcome its distance R from the center (Blustin et al. 2005). Analytically, this condition is

$$\frac{\Delta r}{R} \approx \frac{N_H}{f n_H R} = \frac{\xi R N_H}{L_{ion} f} \leq 1. \tag{2}$$

From Eq. (2), we derived: $R \lesssim 15$ kpc. We note that this distance is well within the typical extension of a galactic halo (e.g., as mapped by H I emission for a large sample, de Blok et al. 2008). Therefore, we use this estimation in the following to derive hard upper limits for the mass outflow rate and kinetic luminosity.

The outflow mass rate is given by

$$\dot{M}_{out} = 4\pi\mu m_P R v N_H C_g = [4-16] \, M_\odot \, \text{yr}^{-1}, \tag{3}$$

where $\mu = 1.4$ is the mean atomic mass per proton and m_P is the proton mass. We assumed a covering factor $C_g = 0.5$, given by the fact that outflows are seen in about 50% of the observed Seyfert galaxies (Dunn et al. 2007).

This value may be compared with the classical mass accretion rate of a black hole in the Eddington regime ($\dot{M}_{Edd} = L_{bol}/\eta c^2$) to obtain an estimation of the impact of the mass loss due to the outflow on the AGN. Assuming a typical accretion efficiency $\eta = 0.1$ and taking $L_{bol} = 9 \times 10^{45}$ erg s^{-1}, as estimated from the SED (see Sect. 3), we obtained

$$\dot{M}_{Edd} \approx 2 M_\odot \, \text{yr}^{-1}. \tag{4}$$

As found in most cases (see Costantini 2010), the mass outflow rate can be of on the same order of the mass accretion rate, suggesting a balance between accretion and ejection in this system. The kinetic luminosity of the outflow is

$$L_{kin} = \frac{\dot{M}_{out} v^2}{2} \approx 10^{40.7-41.4} \, \text{erg s}^{-1}, \tag{5}$$

and it represents a low fraction ($\lesssim 10^{-2}\%$) of the AGN bolometric luminosity L_{bol}. Thus, the outflow is not energetically significant in the AGN feedback scenario, where kinetic luminosities of a few percent of the bolometric luminosities are required (Scannapieco & Oh 2004). We finally estimated the maximum kinetic energy that the outflow can release into the interstellar medium in the case that it is steady all over the AGN life time ($\sim 4 \times 10^8$ yr, Ebrero et al. 2009):

$$E_{tot} \approx 10^{56.8-57.5} \, \text{erg}. \tag{6}$$

As argued in Krongold et al. (2010), this value may in principle be sufficient to evaporate the interstellar environment out of the host galaxy. However, it is not trivial to couple this energy effectively to the galaxy (e.g. King 2010).

7.2. The origin of the emission lines

The simultaneous HST-COS and *XMM-Newton* observation of 1H0419-577 provided a set of narrow lines, ranging from the optical to the X-ray domain, suitable for photoionization modeling. We show that a single gas model cannot account simultaneously for all the narrow line emission. The UV lines are emitted by moderately ionized gas, intercepting about the 10% of the total AGN radiation field. This value for the covering factor is consistent with what previously was reported ($C_v = 1.9\%$–20.5%, Baskin & Laor 2005). The X-ray lines are instead emitted in a more highly ionized gas phase: ($\log \xi \approx 1.44$). We also found that a gas with the same column density and covering factor as the UV emitter is a good description of the X-ray emission. This may suggest that the two emitters are two adjacent layers of the same gas.

Most of the optical emission is not accounted for by our model: it can explain only up to 4% of the Hβ luminosity and 0.3% of [O III] luminosity. Lower densities are required to emit the [O III] lines: the [O III] λ5007 Å line is indeed collisionally de-excited for $n_H \gtrsim 10^5$ cm^{-3} (Osterbrock 1989). Our simple photoionization model cannot however account for the variety of gas physical conditions occurring in the narrow-line region. Our analysis suggests that the NLR is a stratified environment hosting a range of different gas components. Previous studies have shown that multicomponent photoionization models are required for describing the narrow emission lines spectrum of AGN. The narrow line emission from the infrared to the UV is well reproduced assuming that the emitting region consists of clouds with a wide range of gas densities and ionization parameters (Ferguson et al. 1997). In the case of NGC 4151, more than one gas component, with different covering factor, is required to explain line emission even limiting the analysis to the soft X-ray regime (Armentrout et al. 2007). In the present case, the data quality did not allow us to test a more complex, multicomponent scenario.

The estimated gas parameters of the WA are largely inconsistent with the emitters. Thus, neither the UV nor the X-ray emitter can be regarded as the emission counterpart of the WA. Therefore, a connection between the WA and the gas in the NLR is discarded in the present case.

7.3. The geometry of the gas

The present analysis of the UV and X-ray spectrum of 1H0419-577 revealed three distinct gas phases: the UV/X-ray WA, the X-ray emitter ($\log \xi_X \approx 1.44$), and the UV emitter ($\log \xi_{UV} \approx 0.48$). We used the line width of Table 4 to estimate qualitatively the location of the emitters. Assuming that the NLR gas is moving in random keplerian orbits with an isotropic velocity distribution, the velocity v_{FWHM} by which the narrow lines are broadened is given by (Netzer 1990):

$$v_{FWHM} = \sqrt{\frac{4GM}{3R}}, \tag{7}$$

where M is the mass of the SMBH and R is the radial distance from it. The FWHM of the UV lines ([488–805] km s^{-1}, Table 4) therefore give the approximate location of the UV emitter:

$$R_{UV}^{em} \approx [1-3]\,\text{pc}. \tag{8}$$

This distance would imply a gas number density of $n_H = (L_{ion}\xi_{UV})/(R_{UV}^{em})^2 \approx 10^{7-8}$ cm^{-3} at the location of the UV emitter, which is consistent with the range of gas density and distance where these lines are optimally emitted (Ferguson et al. 1997). The X-ray emitter is consistent to be a gas with covering factor and column density similar to the UV emitter. This suggests that it may be a layer of gas adjacent to UV emitter. The higher X-ray ionization parameter may by both produced by a smaller distance to the SMBH and a lower gas density. The gas density in the NLR ionization cone has a smoothly decreasing radial profile (Bianchi et al. 2006). Therefore, a similar gas density for both the emitters can be assumed if the UV and X-ray emitter are not radially detached, as we suggested. From the definition of ionization parameter, it follows that

$$R_X^{em} \approx \sqrt{\frac{\xi_{UV}}{\xi_X}} R_{UV}^{em} \approx [0.3-1.0]\,\text{pc}.$$

This estimation is consistent with the lower limit for the distance ($R_X^{em} \gtrsim 0.1$ pc) that is implied by the upper limit for the broadening of the O VII-f line. This first order estimation places the emitters on a very different distance scale compared to the absorber, again arguing against a connection between emission and absorption in this source. We did not detect the NLR in absorption: this may indicate that the NLR ionization cone is not along our line of sight, as this would produce visible O VII absorption lines. We are possibly detecting scattered light from the NLR. The presence of a circumnuclear scattering region has been proposed, such as for the case of NGC 4151 (Kraemer et al. 2001).

8. Summary and conclusions

We analyzed and modeled the X-ray, UV, and optical data of the Seyfert 1.5 galaxy 1H0419-577. Simultaneous X-ray (RGS) and UV (HST-COS) spectra of the source were taken to study the absorbing-emitting photoionized gas in this source. Optical data from the OM were also used for the present analysis. We found three distinct gas phases with different ionization.

The X-ray and the UV spectrum are both absorbed by the same, lowly ionized WA ($\log \xi = 0.03 \pm 0.15$). The outflow is likely to be located in the host galaxy at a distance $R \gtrsim 4$ kpc from the central source. The kinetic luminosity of the outflow is a low fraction ($\lesssim 10^{-2}$%) of the AGN bolometric luminosity, making the outflow unimportant for the AGN feedback. However, this galactic-scale X-ray absorber, like the one we serendipitously discovered in this source, might still play a role in the host galaxy evolution.

We performed photoionization modeling of the narrow lines emitter using the available UV, X-ray, and optical narrow emission lines. The analysis indicates that the narrow line emitters are not the emission counterpart of the WA. A connection between the WA and the NLR can therefore be discarded in this case.

The X-ray emission lines are emitted in a more highly ionized gas phase compared to the one producing the UV lines. We suggest a geometrical connection between the UV and the X-ray emitter, where the emission takes place in a single gas layer, that is located at about a ∼pc scale distance from the center. In this scenario, the X-ray lines are emitted in a portion of the layer located closer to the SMBH.

Finally, our analysis suggests that the NLR is a stratified environment, hosting a range of gas phases with different ionization and density.

References

Antonucci, R. 1993, ARA&A, 31, 473
Arav, N., Gabel, J. R., Korista, K. T., et al. 2007, ApJ, 658, 829
Armentrout, B. K., Kraemer, S. B., & Turner, T. J. 2007, ApJ, 665, 237
Baskin, A., & Laor, A. 2005, MNRAS, 358, 1043
Bautista, M., Arav, N., Dunn, J., et al. 2009, in BAAS, 41, Am. Astron. Soc. Meet. Abstr., 213,
Behar, E., Rasmussen, A. P., Blustin, A. J., et al. 2003, ApJ, 598, 232
Bianchi, S., Guainazzi, M., & Chiaberge, M. 2006, A&A, 448, 499
Blustin, A. J., Page, M. J., Fuerst, S. V., Branduardi-Raymont, G., & Ashton, C. E. 2005, A&A, 431, 111
Borguet, B. C. J., Edmonds, D., Arav, N., Dunn, J., & Kriss, G. A. 2012, ApJ, 751, 107
Costantini, E. 2010, Space Sci. Rev., 157, 265
Costantini, E., Kaastra, J. S., Arav, N., et al. 2007, A&A, 461, 121
Crenshaw, D. M., & Kraemer, S. B. 1997, in BAAS, 29, Am. Astron. Soc. Meet. Abstr., 1334
Crenshaw, D. M., Kraemer, S. B., & George, I. M. 2003, ARA&A, 41, 117
de Blok, W. J. G., Walter, F., Brinks, E., et al. 2008, AJ, 136, 2648
den Herder, J. W., Brinkman, A. C., Kahn, S. M., et al. 2001, A&A, 365, L7
Detmers, R. G., Kaastra, J. S., & McHardy, I. M. 2009, A&A, 504, 409
Dunn, J. P., Crenshaw, D. M., Kraemer, S. B., & Gabel, J. R. 2007, AJ, 134, 1061
Dunn, J. P., Bautista, M., Arav, N., et al. 2010, ApJ, 709, 611
Ebrero, J., Mateos, S., Stewart, G. C., Carrera, F. J., & Watson, M. G. 2009, A&A, 500, 749
Ebrero, J., Costantini, E., Kaastra, J. S., et al. 2010, A&A, 520, A36
Ebrero, J., Kriss, G. A., Kaastra, J. S., et al. 2011, A&A, 534, A40
Edmonds, D., Borguet, B., Arav, N., et al. 2011, ApJ, 739, 7
Faucher-Giguère, C.-A., & Quataert, E. 2012, MNRAS, 425, 605
Ferguson, J. W., Korista, K. T., Baldwin, J. A., & Ferland, G. J. 1997, ApJ, 487, 122
Ferland, G. J., Korista, K. T., Verner, D. A., et al. 1998, PASP, 110, 761
Ferland, G. J., Martin, P. G., van Hoof, P. A. M., & Weingartner, J. C. 2003 [arXiv:astro-ph/0311520]
Hamann, F. W., Barlow, T. A., Chaffee, F. C., Foltz, C. B., & Weymann, R. J. 2001, ApJ, 550, 142
Hopkins, P. F., Hernquist, L., Cox, T. J., & Kereš, D. 2008, ApJS, 175, 356
Hutsemékers, D., Hall, P. B., & Brinkmann, J. 2004, A&A, 415, 77
Kaastra, J. S., Mewe, R., & Nieuwenhuijzen, H. 1996, in UV and X-ray Spectroscopy of Astrophysical and Laboratory Plasmas, eds. K. Yamashita, & T. Watanabe, 411
Kaastra, J. S., Raassen, A. J. J., Mewe, R., et al. 2004, A&A, 428, 57
Kaastra, J. S., Petrucci, P.-O., Cappi, M., et al. 2011, A&A, 534, A36
Kalberla, P. M. W., Burton, W. B., Hartmann, D., et al. 2005, A&A, 440, 775
Kaspi, S., Brandt, W. N., George, I. M., et al. 2002, ApJ, 574, 643
King, A. R. 2010, MNRAS, 402, 1516
Kraemer, S. B., Crenshaw, D. M., Hutchings, J. B., et al. 2001, ApJ, 551, 671

Kraemer, S. B., Crenshaw, D. M., George, I. M., Gabel, J. R., & NGC 4151
   Team 2005, in BAAS, 37, Am. Astron. Soc. Meet. Abstr., 1190
Kriss, G. A., Arav, N., Kaastra, J. S., et al. 2011, A&A, 534, A41
Krongold, Y., Elvis, M., Andrade-Velazquez, M., et al. 2010, ApJ, 710, 360
Mason, K. O., Breeveld, A., Much, R., et al. 2001, A&A, 365, L36
Mauch, T., Murphy, T., Buttery, H. J., et al. 2003, MNRAS, 342, 1117
McNamara, B. R., & Nulsen, P. E. J. 2012, New J. Phys., 14, 055023
Moe, M., Arav, N., Bautista, M. A., & Korista, K. T. 2009, ApJ, 706, 525
Netzer, H. 1990, in Active Galactic Nuclei, eds. R. D. Blandford, H. Netzer,
   L. Woltjer, T. J.-L. Courvoisier, & M. Mayor, 57
Nucita, A. A., Guainazzi, M., Longinotti, A. L., et al. 2010, A&A, 515, A47
Osterbrock, D. E. 1989, Astrophysics of gaseous nebulae and active galactic
   nuclei (Mill Valley, CA: University Sience Books)
Piconcelli, E., Jimenez-Bailón, E., Guainazzi, M., et al. 2005, A&A, 432, 15
Porquet, D., & Dubau, J. 2000, A&AS, 143, 495
Pounds, K. A., Reeves, J. N., Page, K. L., & O'Brien, P. T. 2004a, ApJ, 605, 670

Pounds, K. A., Reeves, J. N., Page, K. L., & O'Brien, P. T. 2004b, ApJ, 616,
   696
Protassov, R., van Dyk, D. A., Connors, A., Kashyap, V. L., & Siemiginowska,
   A. 2002, ApJ, 571, 545
Scannapieco, E., & Oh, S. P. 2004, ApJ, 608, 62
Scott, J. E., Kriss, G. A., Lee, J. C., et al. 2005, ApJ, 634, 193
Sijacki, D., Springel, V., Di Matteo, T., & Hernquist, L. 2007, MNRAS, 380, 877
Somerville, R. S., Hopkins, P. F., Cox, T. J., Robertson, B. E., & Hernquist, L.
   2008, MNRAS, 391, 481
Steenbrugge, K. C., Kaastra, J. S., Crenshaw, D. M., et al. 2005, A&A, 434, 569
Strüder, L., Briel, U., Dennerl, K., et al. 2001, A&A, 365, L18
Tombesi, F., Cappi, M., Reeves, J. N., et al. 2013, MNRAS, 430, 1102
Turner, M. J. L., Abbey, A., Arnaud, M., et al. 2001, A&A, 365, L27
Turner, T. J., Miller, L., Kraemer, S. B., Reeves, J. N., & Pounds, K. A. 2009,
   ApJ, 698, 99
Véron-Cetty, M.-P., & Véron, P. 2006, A&A, 455, 773